JOURNAL OF SOLID STATE CHEMISTRY 110, 370–383 (1994)

Polarized Optical Absorption Spectroscopy of the $Tl_2MnF_5 \cdot H_2O$ 1D Manganese (III) Single Crystal

F. Rodríguez,*,[1] P. Nuñez,† and M. C. Marco de Lucas*

*DCITTYM (Sección Ciencia Materiales), Facultad Ciencias, Universidad de Cantabria, 39005-Santander, Spain; †Departamento de Química Inorgánica, Universidad de La Laguna, 38200 Tenerife, Spain

Received May 24, 1993; in revised form September 7, 1993; accepted September 15, 1993

The polarized optical absorption spectra of the 1D manganese (III) fluoride $Tl_2MnF_5 \cdot H_2O$ are investigated in the 9.5 –300 K temperature range. Throughout the work, special emphasis is placed on the correlation between the different spectroscopic parameters and the structural and magnetic properties of the title compound. Three prominent, strongly polarized broadbands are observed at 11,700, 17,500, and 20,800 cm^{-1}, which are assigned to the spin-allowed crystal field bands within the d^4 electronic configuration of the Jahn–Teller elongated MnF_6^{3-} complex (D_{4h}). Both the polarization and the temperature dependence of the oscillator strengths indicate that these bands are electric-dipole-assisted by odd parity vibrations, whereas the spin-forbidden transitions are induced by a pairwise exchange mechanism. A salient feature of the present work is the observation of vibronic progressions to a_{1g} modes of 525, 505, and 375 cm^{-1} in the low temperature spectra of the $^5B_{1g} \rightarrow {}^5A_{1g}$ and $^5B_{2g}$ bands. The nature of these modes and the experimental Huang–Rhys factors are analyzed in terms of the linear electron–phonon coupling coefficients, which are derived by correlating the optical spectra of several fluorides with the local geometry around the Mn(III). The presence of an exciton magnon peak in the low temperature spectra is also noteworthy. The temperature dependence of the intensity of this peak as well as of the spin–forbidden transitions provides evidence of magnetic ordering below $T_N = 28$ K and allows us to estimate an intrachain exchange constant of $J = 11$ cm^{-1}.

1. INTRODUCTION

The family of manganese (III) fluoride crystals offers a wide variety of structural and magnetic properties which have been studied extensively in order to establish magnetostructural correlations (1–14). Their crystallographic structure and particularly their dimensionality are greatly influenced by the chemical stoichiometry, favoring the formation of chains $[MnF_4F_{2/2}]$ or layers $[MnF_2F_{4/2}]$ of the F-shared MnF_6^{3-} octahedra depending on whether the formula is A_2MnF_5 (or $BMnF_5$) (8–11) or $AMnF_4$ (7, 12–14) (A and B are mono- and divalent cations, respectively). In A_3MnF_6 (or $ABMnF_6$), a network (hereafter called 0D) of isolated MnF_6^{3-} octahedra is formed (15–17). In all cases, the MnF_6 octahedra display elongated D_{4h} type distortions due to the Jahn–Teller (JT) effect of the Mn (III) (d^4 high spin configuration) which appear enhanced in low-dimensional systems by crystal anisotropy. This situation is clearly evidenced by comparing this distortion in different crystal families. If we denote such a distortion by the parameter x_D defined as $x_D = (R_{ax}/R_{eq}) - 1$, with R_{ax} and R_{eq} being the axial and equatorial Mn–F distances, then x_D decreases with the dimensionality and has values of 0.17, 0.14, and 0.09 for 2D $KMnF_4$ (13), 1D $(NH_4)_2MnF_5$ (10), and 0D Na_3MnF_6 (17), respectively.

This anisotropy at the manganese site, together with the type of bridging among MnF_6^{3-} octahedra, has a large influence on the magnetic ordering of these systems, which can be ferromagnetic (1, 18), weak ferromagnetic (19), or mostly antiferromagnetic. In this respect, it is worth mentioning the investigations carried out on the $A_2MnF_5 \cdot H_2O$ family of linear $[MnF_4F_{2/2}]$ chains whose range of Mn–F–Mn bridging angles and Mn–Mn distances allowed a clear correlation to be established between structural parameters and the intrachain exchange constant (4–6, 9, 20–25).

To date, few studies have attempted to correlate the optical spectra of these materials with their structural and magnetic properties. In fact, most of the optical studies have been performed using diffuse reflectance on powder samples where the fine features of the optical spectra are usually missed (1, 26–30).

The aim of the present work is to investigate the optical properties of the 1D $Tl_2MnF_5 \cdot H_2O$ crystal. Emphasis has been placed on the d^4 intraconfigurational transitions of the Mn (III), which are highly polarized by the large distortion of the MnF_6 octahedra ($x_D = 0.136$). This aspect is clearly evidenced by these crystals, in which the color varies from purple to yellow-green depending on whether the electric vector of the polarized light is perpendicular or parallel to the chain.

[1] To whom correspondence should be addressed.

0022-4596/94 $6.00

The synthesis of good optical-quality single crystals allowed us to investigate aspects which are not usually studied in these Mn (III) compounds. In particular, the temperature dependence of the oscillator strengths of both the spin-forbidden and spin-allowed electric-dipole transitions and the electron–phonon couplings have been analyzed in detail. Attention has also been paid to the sharp features observed at low temperatures in the region of the spin-forbidden transitions, which in the case of the isoelectronic Cr^{2+} ion in the insulating ferromagnet K_2CrCl_4 are known to be very sensitive to the magnetic ordering (31). A salient result of this work is the correlation we have established between the transition energies of the crystal field bands and the local geometry around the Mn (III). This is relevant in explaining the electron–phonon couplings experimentally observed in the title compound.

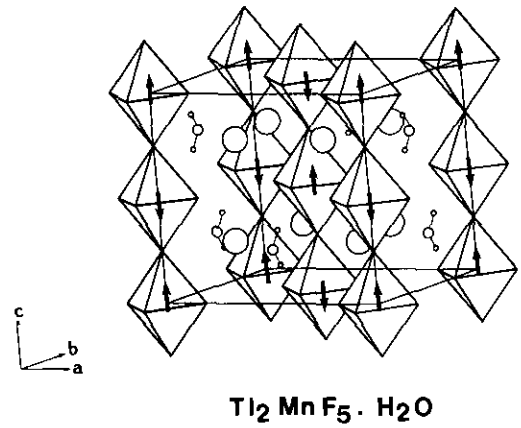

FIG. 1. Nuclear and magnetic structures of the $Tl_2MnF_5 \cdot H_2O$ crystal. Octahedra, arrows, and large circles represent MnF_6^{3-} units, Mn(III) spin direction, and Tl(I) ions, respectively.

2. EXPERIMENTAL

2a. Synthesis of $Tl_2MnF_5 \cdot H_2O$ and its Crystallographic and Magnetic Structures

Single crystals of $Tl_2MnF_5 \cdot H_2O$ were grown from cold solutions of Mn(III) and Tl(I) fluorides in hydrofluoric acid following the method reported elsewhere (9).

This solid is orthorhombic (*Cmcm* space group) with lattice parameters $a = 9.688$ (2) Å, $b = 8.002$ (1) Å, and $c = 8.339$ (1) Å at room temperature. As is shown in Fig. 1, the structure consists of linear chains of *trans*-connected $[MnF_4F_{2/2}]$ octahedra along the **c** direction. The octahedra display a nearly D_{4h} symmetry. The axial and equatorial Mn–F distances are 2.082 and 1.832 Å, respectively. The equatorial distance actually corresponds to the average of the 1.818 and 1.845 Å Mn–F distances along the **a** and **b** directions, respectively.

It is worth noting that the Mn–F–Mn angle, $\beta = 179.2°$, is close to 180°, which is important for polarized optical studies. The water molecules lie in (100) planes with the twofold axis perpendicular to **c**, and connect two neighboring octahedra of the same chain, forming zigzag rows parallel to the octahedral chain, as is shown in Fig. 1.

Magnetic and neutron diffraction measurements indicate that $Tl_2MnF_5 \cdot H_2O$ is antiferromagnetic with an intrachain exchange constant, $J = 15$ cm^{-1}. A 3D magnetic ordering with the spins parallel to **c** occurs below $T_N = 28$ K.

2b. Optical Absorption Spectra

Single crystals of about $1 \times 0.5 \times 0.2$ mm^3 with elongated parallelopipedal habits along the **c** direction were used for the optical absorption (OA) spectra. Spectra were recorded with a Lambda 9 Perkin–Elmer spectrophotometer equipped with Glan Taylor polarizing prisms. The polarized light propagates perpendicularly to **c** with **E** parallel (π) or perpendicular (σ) to the chain (**c** direction).

The temperature was stabilized to within 0.05 K in the 9.5–300 K range with a Scientific Instruments 202 closed circuit cryostat and an APD-K controller.

Infrared spectra in the 220–4000 cm^{-1} range were obtained with a Nicolet 710-FT IR spectrometer. Suitable KBr pellets of $Tl_2MnF_5 \cdot H_2O$ and Na_2MnF_5 powders were used.

Transition energies have been calculated by means of the program package of Yeung and Rudowicz (32), kindly provided by the authors through J. A. Aramburu.

3. RESULTS

Figure 2 shows the polarized OA spectra at 298 K of single crystals of $Tl_2MnF_5 \cdot H_2O$ in the 4000–28,000 cm^{-1} range. The variations of optical density between 15,000 and 20,000 cm^{-1} are responsible for the marked dichroism

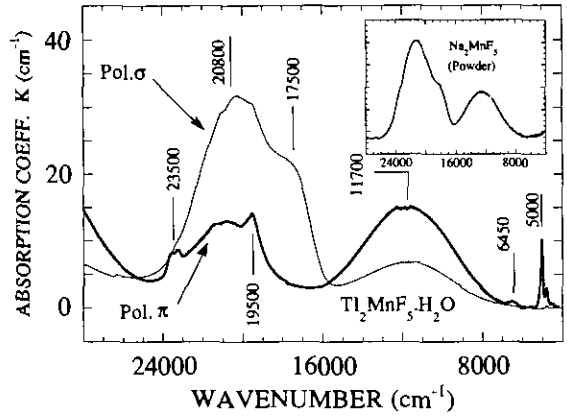

FIG. 2. Polarized OA spectra of the $Tl_2MnF_5 \cdot H_2O$ crystal at $T = 297$ K.

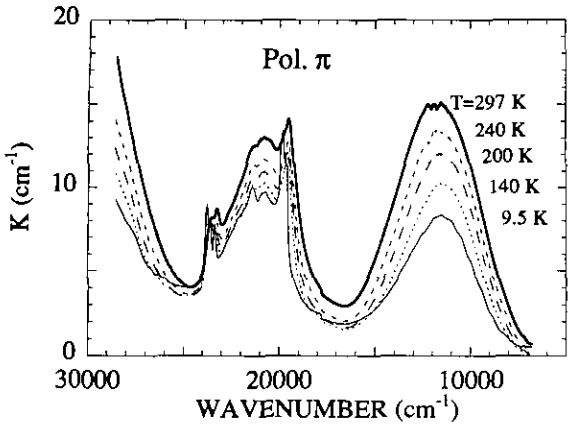

FIG. 3. Temperature dependence of the π polarized OA spectra.

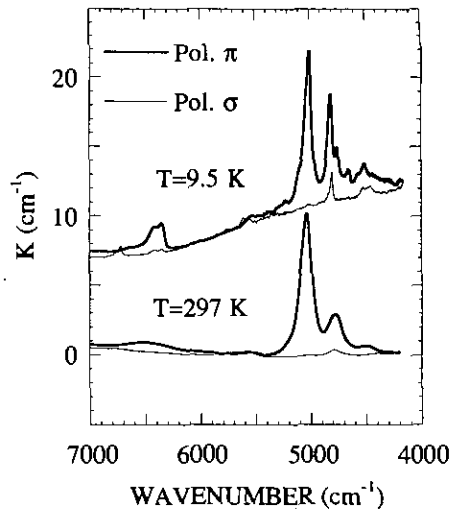

FIG. 5. Polarized OA spectra in the 4000–7000 cm^{-1} range at T = 9.5 K and 297 K. For the sake of clarity, the low temperature spectra have been displaced.

exhibited by this crystal. For comparison purposes, the OA spectrum of a Na_2MnF_5 powder is included in the inset. This comparison is of particular interest for clarifying the contribution of the water molecules to the OA spectra of $Tl_2MnF_5 \cdot H_2O$.

The bands at 5000, 6450, and 17,500 cm^{-1} are completely polarized either π or σ, while the bands at 11,700 and 20,800 cm^{-1} appear in both π and σ polarizations. The intensity of the 11,700 cm^{-1} band is higher in π polarization, while the opposite occurs for the 20,800 cm^{-1} band. There are narrow bands at 19,500 and 23,500 cm^{-1} which are only observed in the π spectrum. It is interesting to observe the extremely large bandwidth of the 11,700 cm^{-1} band, H = 4200 cm^{-1}, in comparison to those of the 17,500 and 20,800 cm^{-1} bands, for which the bandwidths at room temperature are about 2000 and 3500 cm^{-1}, respectively.

The temperature dependence of the π and σ spectra is illustrated in Figs. 3 and 4. The low temperature spectra of the 6450 and 5000 cm^{-1} bands are shown in Fig. 5.

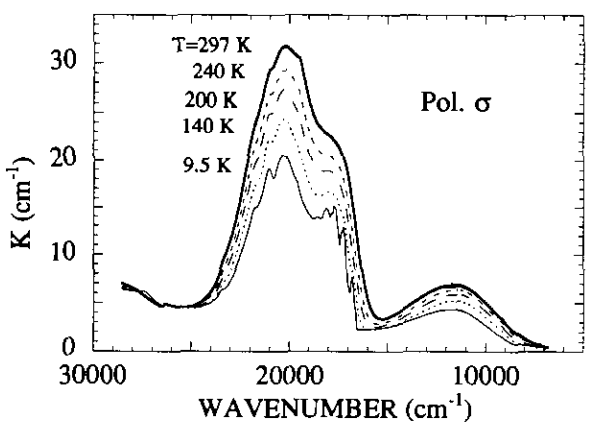

FIG. 4. Temperature dependence of the σ polarized OA spectra.

The origin of these bands is discussed separately in the appendix. The most relevant features of these temperature-dependent variations are summarized in the following points.

(1) The integrated intensity of the 11,700, 17,500, and 20,800 cm^{-1} broad bands decreases continuously upon cooling. By contrast, the intensity of the narrow bands at 19,500 and 23,500 cm^{-1} is almost unaffected in the whole 9.5–300 K temperature range. The corresponding intensity variations, $I(T)$, are depicted in Fig. 6. Actually, we represent the transition oscillator strengths, $f(T)$, which are related to $I(T)$ for ED transitions through the equation (33)

$$f(T) = \frac{1.018 \times 10^{13}}{N} \frac{n}{(n^2+2)^2} I(T), \qquad [1]$$

where $I(T) = \int_{\text{Band}} K(E)\, dE$; $K(E)$ is the absorption coefficient (cm^{-1}), E the wavenumber (cm^{-1}), $N = 6.19 \times 10^{21}$ cm^{-3}, and n = 1.67 is the refractive index measured by the Becke line method.

It should be noted that $f(T)$ for the 11,700 cm^{-1} band increases about twofold in both polarizations on going from 9.5 to 300 K. Although this temperature dependence is difficult to obtain for the 17,500 and 20,800 cm^{-1} broadbands because of their large overlap, we have roughly estimated their respective integrated intensities in both polarizations by fitting the OA spectra in the 16,000–25,000 cm^{-1} range to the sum of two gaussians. This analysis shows that the area of the individual gaussians at 300 K is also about twice the area at low temperature for both bands and both polarizations. Figure 6 also shows the temperature dependence of the bandwidth $H(T)$ of

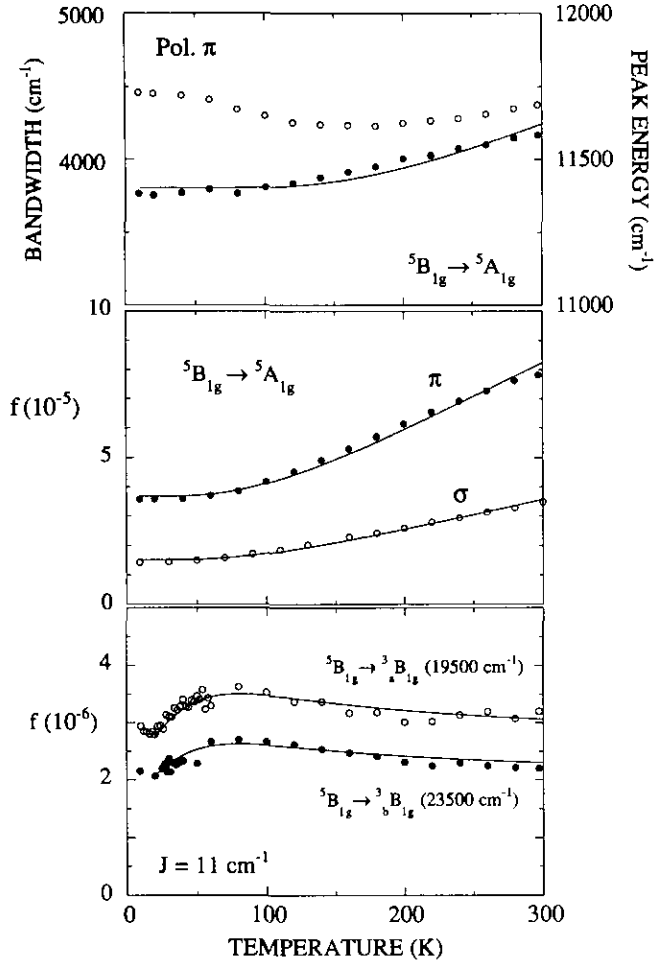

FIG. 6. (Top) Temperature dependence of the bandwidth and peak energy of the $^5B_{1g} \rightarrow {}^5A_{1g}$ band at 11,700 cm^{-1} in π polarization. Solid line is the fitting of the bandwidth to the equation $H(T) = H_0[\coth(\hbar\omega_{ef}/2K_BT)]^{1/2}$ with $H_0 = 3700$ cm^{-1} and $\hbar\omega_{ef} = 460$ cm^{-1}. (Middle) Variation of the oscillator strength of the $^5B_{1g} \rightarrow {}^5A_{1g}$ band in the σ and π polarizations. Solid lines are fittings to Eq. [2]. (Bottom) Variation of the oscillator strength of the two $^5B_{1g} \rightarrow {}^3B_{1g}$ narrow bands in π polarization. Solid lines are fittings to Eq. [3] for $J = 11$ cm^{-1} and $f(0) = 2.0 \times 10^{-6}$ and 1.5×10^{-6} for ${}^3_aB_g$ and ${}^3_bB_{1g}$, respectively.

the 11,700 cm^{-1} band, which was obtained from the second order moment $M2$ through $H = 2.36\sqrt{M2}$, as well as the variation of the first order moment $M1$.

(2) A rich vibrational structure is observed in the 11,700 and 17,500 cm^{-1} bands at low temperatures. The broadband at 11,700 cm^{-1} displays a large progression with an average vibrational spacing of 525 cm^{-1} in the π spectrum at $T = 9.5$ K (Fig. 7). Such a progression is clearly seen in the second derivative spectrum, where 16 components formed from the origin at $E_0 = 7240$ cm^{-1} are detected. Actually, these components are not equally spaced but their energies, E_n, fit to the formula: $E_n = 7240 + 543\,n - 1.21\,n^2$, which gives evidence of anharmonic effects.

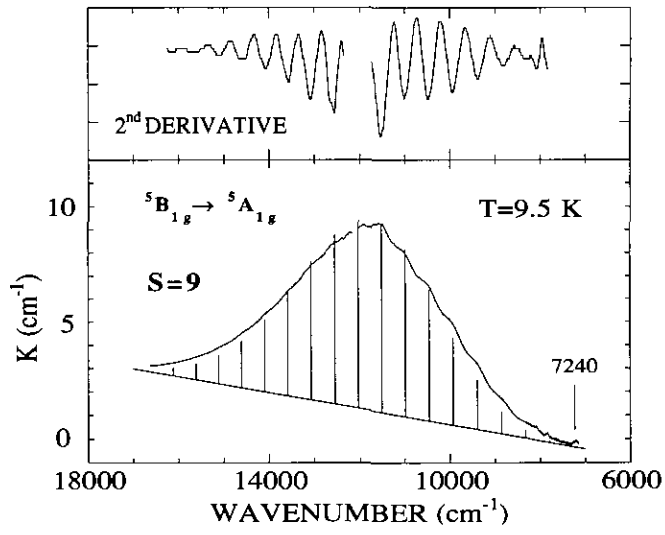

FIG. 7. Vibrational structure of the $^5B_{1g} \rightarrow {}^5A_{1g}$ band at $T = 9.5$ K. Figures at the bottom and the top show the π spectrum and the corresponding 2nd derivative spectrum. Vertical lines in each component of the progression represent the Pekarian intensity distribution according to Eq. [4].

The intensity of nth-component of the progression can be described well by a Pekarian distribution, $I(E_0 + n\hbar\omega) = I_0S^n/n!$, with $S = 9.0$.

Below 100 K, another progression of 435 cm^{-1} is observed in the 17,500 cm^{-1} band in σ-polarization, although in this case it shows a more complex structure and only four components are detected. Just below 30 K, a rich fine structure appears upon this progression. Figure 8

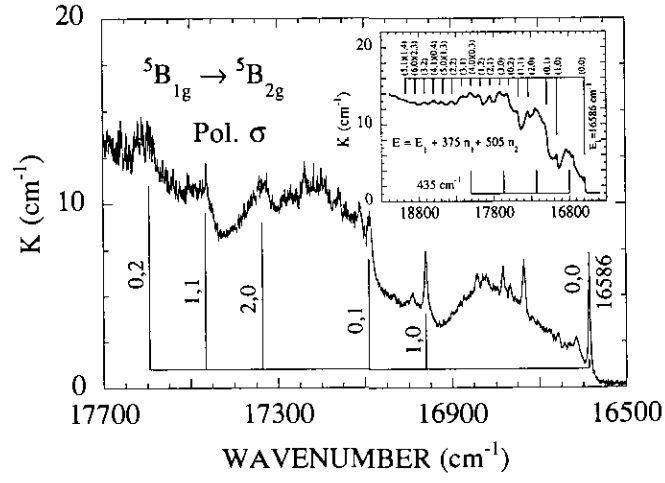

FIG. 8. Vibrational structure of the $^5B_{1g} \rightarrow {}^5B_{2g}$ band at $T = 9.5$ K. The σ spectrum shows the first 1000 cm^{-1} above the origin at $E_1 = 16{,}586$ cm^{-1}. Spectral resolution $\Delta\lambda = 0.8$ Å. The inset shows the whole band (spectral resolution $\Delta\lambda = 3$ Å). In both spectra, vertical lines are placed at energies $E(n_1, n_2) = E_1 + 375n_1 + 505n_2$, associated with the transition between vibronic states $^5B_{1g}$ (0, 0) and $^5B_{2g}$ (n_1, n_2). The vibrational energies of the coupled modes are 375 and 505 cm^{-1}, respectively.

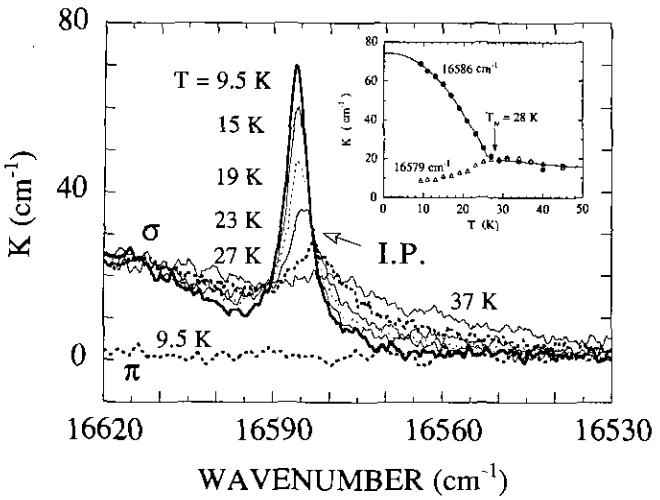

FIG. 9. Temperature dependence of the σ polarized $^5B_{1g} \rightarrow {}^5B_{2g}$ band around the electronic origin. The corresponding π spectrum at $T = 9.5$ K is also included. Spectral resolution $\Delta\lambda = 0.8$ Å. The inset shows the variation of the absorption coefficient at 16,586 and 16,579 cm^{-1} in the 9.5–50 K range. The solid line below 25 K represents a T^2-type behavior.

shows the spectrum at $T = 9.5$ K above the origin of this band. A noteworthy feature of this spectrum is the sharp peak ($H = 10$ cm^{-1}) observed at $E_1 = 16{,}586$ cm^{-1} in the origin of this band. The weak peak structure extending over 100 cm^{-1} above this origin is probably associated with low energy lattice modes. This structure is also reproduced in the two sharp peaks located 150 and 200 cm^{-1} above the origin as well as in the more prominent peak at 375 cm^{-1}. A phonon sideband corresponding to the first component of the progression is formed from the origin. The sharp features of this band are observed as replicas of this E_1 origin and their positions can be described through vibrational spacings of 505 and 375 cm^{-1} by the equation $E(n_1, n_2) = E_1 + 375n_1 + 505n_2$, where n_1 and n_2 are integers. Similar replicas formed from the sharp peaks at $E_1 + 150$ and $E_1 + 200$ cm^{-1} can be guessed from the spectrum of Fig. 8. The inset shows this structure along the whole band.

A salient feature of the sharp peak at 16,586 cm^{-1} concerns its intensity temperature dependence (Fig. 9). The presence of an isosbestic point at 16,583 cm^{-1} probably indicates that *hot* components arise on the low energy side of this peak. However, such components could not be resolved spectroscopically. The variation of the absorption coefficient is represented for two energies above and below the isosbestic point in the inset of Fig. 9. In both cases, the variation reflects anomalies at 25 K. Phenomenological trials fail to explain the thermal dependence of the 16,586 cm^{-1} peak intensity when using Arhenius plots, but a T^2-type dependence accounts well for the experimental behavior below 25 K.

The temperature dependence of the π polarized narrow bands in the 9.5–61 K range is illustrated in Fig. 10. The 23,500 cm^{-1} band shows a fine structure with three peaks at 23,320, 23,560, and 23,730 cm^{-1} and bandwidths of about 70 cm^{-1}. At variance with the sharp line at 16,586 cm^{-1}, the intensity of these peaks is not significantly affected by temperature. Only a broadening and a small redshift of about 20 cm^{-1} are observed in this temperature range. Similar features are found for the narrow band at 19,500 cm^{-1}. However, the variation of the halfwidth, $H_{1/2}(T)$, of the sharp peak at 19,600 cm^{-1} also shows anomalies at $T = 25$ K (inset of Fig. 10).

Finally, the room temperature infrared spectra of both $Tl_2MnF_5 \cdot H_2O$ and Na_2MnF_5 in the 4000–220 cm^{-1} spectral range are depicted in Fig. 11. The peaks at 1648, 3273, and 3375 cm^{-1}, only observed in $Tl_2MnF_5 \cdot H_2O$, are associated with water absorption. Both spectra display a similar structure below 700 cm^{-1}, although it is less complex in the case of $Tl_2MnF_5 \cdot H_2O$ with four peaks at 686, 554, 395, and 277 cm^{-1}.

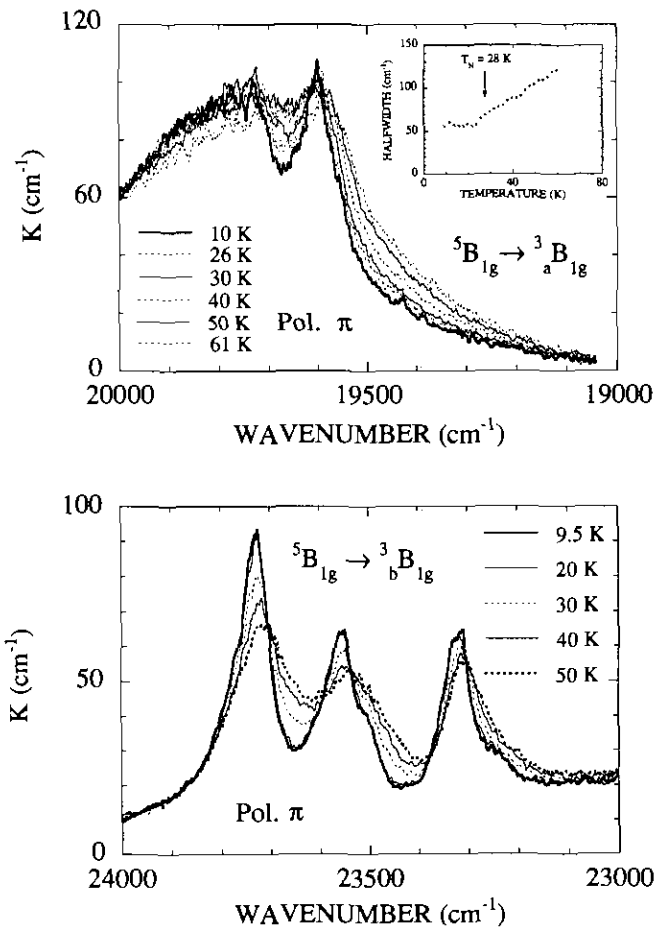

FIG. 10. Temperature dependence of the π polarized $^5B_{1g} \rightarrow {}^3_aB_{1g}$ and ${}^3_bB_{1g}$ narrow bands in the 9.5–61 K range. The inset shows the variation of the halfwidth of the 19,600 cm^{-1} peak with the temperature.

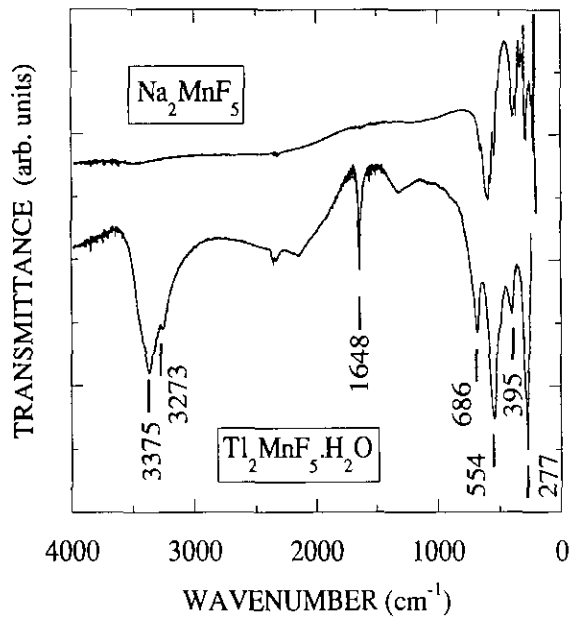

FIG. 11. Room temperature infrared spectra of $Tl_2MnF_5 \cdot H_2O$ and Na_2MnF_5 powders in the 220–4000 cm^{-1} range.

4. ANALYSIS AND DISCUSSION

4a. Assignment of the Optical Absorption Spectrum

The structureless room temperature OA spectra of $Tl_2MnF_5 \cdot H_2O$ (Fig. 2) are very similar to those observed in other bi- or trimetallic manganese (III) fluorides. Table 1 reports the band assignment for $Tl_2MnF_5 \cdot H_2O$ and for several crystals of the A_3MnF_6, A_2MnF_5, and $AMnF_4$ families, together with some relevant structural data.

Within a d^4 electronic configuration, there are three possible spin-allowed electric-dipole (ED) transitions in elongated MnF_6^{3-} complexes (D_{4h} site symmetry). These transitions involve electronic jumps from the one electron $d_{3z^2-r^2}$, d_{xy}, and d_{xz} or d_{yz} orbitals to the unoccupied $d_{x^2-y^2}$ one electron level. As indicated in Table 1, the broad bands at 11,700 (ε_1), 17,500 (ε_2), and 20,800 (ε_3) cm^{-1} of $Tl_2MnF_5 \cdot H_2O$ are assigned to transitions from the ground $^5B_{1g}$ electronic state to the excited spin quintets $^5A_{1g}$, $^5B_{2g}$, and ^5E_g, respectively, following the scheme of Fig. 12.

The transition energy ε_2, which only depends on the equatorial ligand field, gives the $10Dq$(eq) parameter directly, hereafter called simply $10Dq$, while $\Delta_e = \varepsilon_1$ and $\Delta_t = \varepsilon_3 - \varepsilon_2$ represent the tetragonal splitting of the parent ^5E_g and $^5T_{2g}$ octahedral states, respectively. These parameters are related to the tetragonal crystal field parameters D_s and D_t (or e_σ and e_π within the orbital angular overlap model) through the expressions included in Fig. 12 (33). Within the crystal field model, $10Dq$ is equivalent to an octahedral crystal field splitting but taking the equatorial distance, R_{eq}, as the octahedral metal–ligand distance (26). Thus, $10Dq$ varies as R_{eq}^{-5} within this model. Values of $10Dq$, Δ_e, and Δ_t for different MnF_6^{3-} complexes have also been included in Table 1.

A salient feature which can be inferred from Table 1 is the sensitivity of ε_1 to the tetragonal distortion of the MnF_6^{3-} octahedron. In fact, while ε_2 ($10Dq$) lies between 17,500 and 18,500 cm^{-1} for all crystals, ε_1 is around 9000 cm^{-1} for the A_2MnF_6 compounds, 12,000 cm^{-1} for A_2MnF_5, and 15,000 cm^{-1} for $AMnF_4$. This simple result allows us to establish a first correlation between optical and structural properties, i.e., between Δ_e and the crystal dimensionality. It is difficult to make this correlation for $10Dq$ since accuracies in ε_2 of less than 300 cm^{-1} are hard to obtain due to the large overlap between the $^5B_{1g} \rightarrow {}^5B_{2g}$ and $^5B_{1g} \rightarrow {}^5E_g$ bands. However it is worth pointing out that the variation of $10Dq$ throughout this series (1000 cm^{-1}) is much smaller than is expected on the basis of the $10Dq$ dependence on R_{eq}^{-p} with $p = 5$. If such a dependence is assumed, a redshift of about 3000 cm^{-1} should be found on passing from $TlMnF_4$ (1.82 Å) to Na_3MnF_6 (1.88 Å). An exponent p smaller than 5 could account

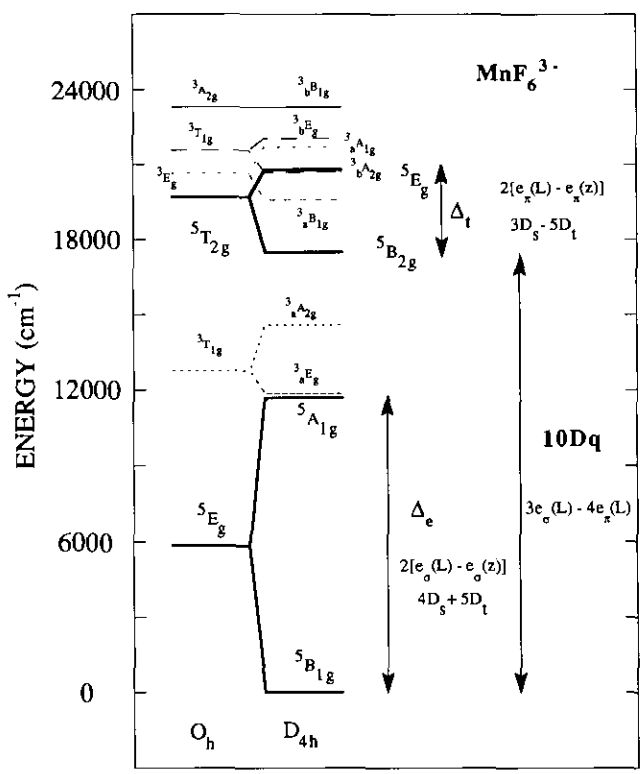

FIG. 12. Energy level diagram of the MnF_6^{3-} complex (high spin d^4 electronic configuration) with elongated D_{4h} symmetry. The energies have been calculated using the same parameters given in Table 2. Expressions relating the tetragonal splitting Δ_t and Δ_e, as well as $10Dq$, with the crystal field parameters, D_s and D_t, and the atomic angular overlap parameters, e_σ and e_π, are included. Symbols L and z denote equatorial and axial ligands, respectively.

TABLE 1
Experimental Transition Energies and the Corresponding Tetragonal (Δ_t and Δ_e) and $10Dq$ Parameters of Different Manganese(III) Fluorides

Compound	$^5B_{1g} \rightarrow {}^5E_g$	$^5B_{2g}$ ($10Dq$)	$^5A_{1g}$ (Δ_e)	$^5B_{2g} \rightarrow {}^5E_g$ (Δ_t)		R_{ax}	R_{eq}	$\langle R_{eq} \rangle$	x_D	Ref.
K_2NaMnF_6	19,500	17,500	9,000	2,000		2.06	1.86	1.86	0.108	[16, 26]
Na_3MnF_6	19,200	17,600	8,400	1,600		2.018	1.862 1.897	1.880	0.074	[17, 1]
$(NH_4)_2MnF_5$	21,000	18,200	12,750	2,800		2.091	1.838 1.842	1.840	0.136	[10, 27]
$Tl_2MnF_5 \cdot H_2O$	20,800	17,500	11,700	3,300		2.082	1.818 1.845	1.832	0.136	[9] Present work
Na_2MnF_5	21,000	18,000	12,500	3,000	(1)	2.114	1.841 1.849	1.845	0.146	[11, 26]
					(2)	2.103	1.829 1.872	1.851	0.136	[11]
$RbMnF_4$	22,500	18,500	15,500	4,000		2.154	1.882 1.805	1.844	0.168	[13, 1]
$KMnF_4$	22,300	18,300	15,400	4,000		2.155	1.87 1.80	1.835	0.174	[13, 1]
$CsMnF_4$	22,000	18,000	15,500	4,000		2.162	1.860 1.821	1.841	0.175	[13, 1]
$TlMnF_4$	22,000	18,200	14,500	3,800		2.146	1.86 1.78	1.82	0.179	[14, 1]

Note. R_{ax}, R_{eq}, and $\langle R_{eq} \rangle$ denote the axial, equatorial, and averaged equatorial F–Mn distances, respectively. x_D is the tetragonal parameter of the MnF_6^{3-} complex. The optical and structural data of each compound were taken from the first and the second reference, respectively. The two types of MnF_6^{3-} complexes in Na_2MnF_5 are indicated. Units in cm^{-1} and Å.

for the experimental $10Dq$ values in MnF_6^{3-}, although R dependencies with $p = 5$ have been found through theoretical calculations in several octahedral transition metal complexes (26, 34–36) and experimentally verified for MnF_6^{4-} complexes in Mn^{2+} doped fluoroperovskites (37–39).

A precise structural correlation can be made for Δ_e and Δ_t since there are important variations of these parameters along the crystal series shown in Table 1 and the *local* structure of the MnF_6^{3-} complexes is known from crystallographic data. In this respect, Fig. 13 shows the variation of Δ_e and Δ_t with the tetragonal parameter x_D. Linear relations $\varepsilon_1 = \Delta_e = 8.8 \times 10^4 x_D$ and $\varepsilon_3 - \varepsilon_2 = \Delta_t = 2.2 \times 10^4 x_D$ are derived from these plots. Note that the ratio $\Delta_e/\Delta_t = 4$ indicates that there is a larger contribution to the splitting of the parent ^5E_g and $^5T_{2g}$ octahedral states from the σ bonding interactions of the e_g ($3z^2 - r^2$, $x^2 - y^2$) orbitals than from the π bonding interactions due to the t_{2g} orbitals. Similar effects are observed in tetragonal *compressed* CuF_6^{4-} (d^9) complexes formed in K_2ZnF_4 (40) and Ba_2ZnF_6 (41), although the ratio $\Delta_e/\Delta_t \sim 3$ is somewhat smaller than for MNF_6^{3-}. Such a reduction must be mainly associated with Δ_e rather than with Δ_t, as has been concluded from the spectroscopic data available for CuF_6^{4-} systems (26, 42). In fact, while ε_1 presents a variation from 7500 to 5800 cm^{-1} between the elongated CuF_2

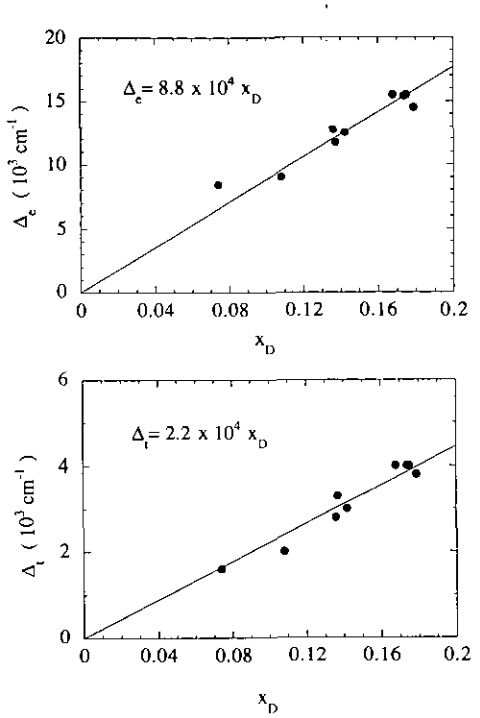

FIG. 13. Variation of Δ_t and Δ_e with the tetragonal parameter, $x_D = R_{ax}/R_{eq} - 1$. Experimental points correspond to the manganese (III) data given in Table 1. The straight lines, $\Delta_e = 8.8 \times 10^4 x_D$ and $\Delta_t = 2.2 \times 10^4 x_D$ (in cm^{-1}) are the least-square fittings.

($x_D = 0.18$) and the compressed $CsAlCuF_6$ ($x_D = -0.12$), respectively, the values of Δ_t vary over a narrower range between 2000 and 3000 cm^{-1} (Tables I and III of Ref. (26)). In line with the discussion in Ref. (41), the enhancement of the Δ_e splitting with respect to Δ_t that we have observed could reflect a weaker σ axial interaction between the a_{1g} ($3z^2 - r^2$) orbital and the metal a_{1g} ($4s$) orbital in the MnF_6^{3-} complexes.

In any case, the present results show that ε_1 provides useful information not only for discerning the 0−, 1−, or 2D character of the MnF_6^{3-} network in these compounds, but also for making a first estimation of the R_{ax}/R_{eq} ratio of MnF_6^{3-} complexes.

The π-polarized narrow bands appearing above 19,000 cm^{-1} (Fig. 2) are assigned to spin-forbidden transitions from the $^5B_{1g}$ ground state to spin-triplet states within the d^4 configuration. Their polarization and temperature dependence allow us to analyze the transition mechanism as well as to confirm the assignment given in Table 2.

Transition energies have been calculated by diagonalizing the Tanabe–Sugano matrices within D_{4th} symmetry including the spin–orbit interaction. The energy diagrams of Fig. 12 and Table 2 show the results of these calculations. Two relevant facts should be pointed out: (1) the experimental peaks at 19,500 and 23,500 cm^{-1} observed π polarization are close to those corresponding to the $^5B_{1g} \rightarrow {}^3{}_aB_{1g}$ and ${}^3{}_bB_{1g}$ transitions, while the σ polarized shoulder at 21,700 cm^{-1} is near to the $^5B_{1g} \rightarrow {}^3{}_bE_g$ or ${}^3{}_aA_{1g}$ transitions; other possible transitions to triplet states are not observed in the OA spectra; (2) suitable values of the zero-field splitting parameter, D, for the $^5B_{1g}$, $^5A_{1g}$, and $^5B_{1g}$ states are obtained from their respective spin–orbit splitting. The calculated values are − 4.6, 8 and 5.0 cm^{-1}, respectively, for a spin–orbit interaction constant of $\zeta = 380$ cm^{-1}. Note that the negative value of D found for $^5B_{1g}$ reflects the existence of an important magnetic anisotropy which plays a relevant role in the magnetic ordering with spins aligned along the c direction in $Tl_2MnF_5 \cdot H_2O$.

TABLE 2

Band Assignment and Calculated and Experimental Transition Energies and Oscillator Strengths of the OA Bands of the $Tl_2MnF_5 \cdot H_2O$ Crystal for π and σ Polarizations at $T = 297$ K

Assignment	Calc. energy	σ Polarization		π Polarization	
		Energy	f (× 10^5)	Energy	f (× 10^5)
$^5B_{1g} \rightarrow {}^5A_{1g}$	11,700	11,600	3.0	11,700	7.5
${}^3{}_aE_g$	12,769	—		—	
${}^3{}_aA_{2g}$	14,583	—		—	
$^5B_{2g}$	17,500	17,500	~3.5	—	0
${}^3{}_aB_{1g}$	19,585			19,500	0.32
^5E_g	20,800	20,300 21,100	~4.0	20,800 21,400	~13.5
${}^3{}_bA_{2g}$	20,666	—		—	
${}^3{}_aA_{1g}$	21,734	21,700 (?)			
${}^3{}_bE_g$	22,095				
${}^3{}_bB_{1g}$	23,307			23,500	0.22

Note. The calculated energies have been obtained using the crystal field parameters $D_s = 2143$ cm^{-1}, $D_t = 626$ cm^{-1}, and $10Dq = 17{,}500$ cm^{-1}; the Racah parameters $B = 780$ cm^{-1} and $C = 3400$ cm^{-1}; and the Trees parameter $\alpha = 70$ cm^{-1}.

4b. Polarization and Temperature Dependence: Transition Mechanisms

4b1. Spin-allowed transitions. The polarization and the temperature dependence of the oscillator strength of the crystal field bands in transition metal complexes are closely related to the transition mechanism. In centrosymmetric complexes, all ED transitions are parity-forbidden and also spin-forbidden if the involved states have different spin multiplicities.

The parity-forbiddenness can be relaxed by noncentrosymmetric distortions of the crystal field, which can be either static or dynamically induced by odd parity vibrations. In the latter case, the transition oscillator strength increases with temperature following a behavior: $f(T) = \Sigma f_i \coth(\hbar\omega_{ui}/2K_BT)$, where f_i is the oscillator strength at 0 K induced by the i^{th} odd parity vibration of energy $\hbar\omega_{ui}$. The summation extends over all odd modes enabling ED oscillator strength. In noncubic systems, these transitions are polarized according to the symmetry of the vibrational mode.

The $^5B_{1g} \rightarrow {}^5A_{1g}$, $^5B_{2g}$, and ^5E_g transitions of the D_{4h} symmetry MnF_6^{3-} complexes are clear examples of this behavior. In the present situation with a linear chain of transconnected MnF_6^{3-} distorted octahedra, there are six possible odd parity modes: three modes with e_u symmetry, two a_{2u} modes and one b_{2u} mode. The a_{2u} modes involve symmetric and antisymmetric stretching motions of the axial Mn–F bond while the corresponding two e_u modes involve similar motions in the equatorial plane. The remaining e_u and b_{2u} modes correspond to antisymmetric bending of the F–Mn–F bonds in the equatorial plane (b_{2u}) and also along the chain (e_u). According to the analysis given in Ref. (27), ED vibronically induced transitions from the $^5B_{1g}$ ground state are polarized either π or σ, depending on whether the product $^5B_{1g} \times \Gamma_u \times {}^5\Gamma_g$ contains the ED operator irreps. a_{2u} or e_u, respectively. In this product, Γ_u and $^5\Gamma_g$ are the symmetries of the vibration and of the electronic excited state, respectively. Therefore, the $^5B_{1g} \rightarrow {}^5A_{1g}$ transition should be π polarized through the b_{2u} mode and σ polarized through the three e_u modes. Transitions to $^5B_{2g}$ would only be σ polarized

through the three e_u modes. Finally in the $^5B_{1g} \rightarrow {}^5E_g$ transition, the e_u modes should induce π polarization, while the two a_{2u} and the b_{2u} modes contribute to the σ polarization. These simple analyses can explain reasonably well the polarization behavior of the spin allowed transitions of Figs. 2, 3, and 4. In particular, it is worth noting the absence of the $^5B_{1g} \rightarrow {}^5B_{2g}$ band in the π spectrum according to the present analysis. Moreover, the fact that the oscillator strength of the first $^5B_{1g} \rightarrow {}^5A_{1g}$ band in π polarization is about twice that in σ polarization clearly suggests that b_{2u} is the most efficient enabling mode in spite of the fact that three e_u modes should be involved in σ polarization. This also seems to occur in the $^5B_{1g} \rightarrow {}^5E_g$ band, for which the higher oscillator strength is observed in the σ spectrum where the b_{2u} mode is involved. This result confirms that bending modes are more efficient for driving ED oscillator strength, as it is usually observed in octahedral systems such as $Cs_2NaYCl_6:Cr^{3+}$ (45), $K_2NaGaF_6:Cr^{3+}$ (46), $Rb_2KGaF_6:Cr^{3+}$ (47), $LiCaAlF_6:Cr^{3+}$ (48), and $KMgF_3:Mn^{2+}$ (49) where the parent t_{2u} mode, with $\hbar\omega_u \sim 200$ cm^{-1} in fluorides, is always involved in the transition mechanism.

The vibronically induced ED character of these transitions is also confirmed by the temperature dependence of the oscillator strength following hyperbolic tangent type behaviors. Solid lines in Fig. 6 represent the fitting to

$$f(T) = f_o \coth(\hbar\omega_u/2K_BT). \quad [2]$$

The fitting parameters are $f_o = 1.5 \times 10^{-5}$ and 3.7×10^{-5}, and $\hbar\omega_u = 200$ and 165 cm^{-1} for σ and π polarizations, respectively. This latter vibrational energy must necessarily correspond to the b_{2u} mode in view of the previous analysis. Similar $\hbar\omega_u$ values are expected for the $^5B_{2g}$ and ^5E_g bands in both polarizations, taking into account the estimated room to low temperature intensity ratios. In addition to reflecting the effectiveness of the b_{2u} mode, the present data also show that the e_u mode corresponding to the octahedral t_{2u} is actually the most efficient among the e_u modes. This conclusion is based on the fact that the experimental temperature dependence is described well simply by using Eq. [2] with a vibrational frequency, $\hbar\omega_u = 200$ cm^{-1}, close to that of the b_{2u} mode. Moreover, the values $\hbar\omega_u = 200$ and 165 cm^{-1} agree with those expected for the lowest frequency e_u and b_{2u} modes and confirm that no other vibrational modes are involved in the transition mechanism because their frequencies would lie well above 200 cm^{-1}. The comparison of the IR peaks of Fig. 11 with the frequencies of several octahedral fluoride complexes supports this view.

Vibrational energies around 500–600 cm^{-1} for a_{1g} and $t_{1u}{}^1$, 400–500 cm^{-1} for e_g, 300–400 cm^{-1} for $t_{1u}{}^2$, and 100–200 cm^{-1} for t_{2u} are found in $[AlF_6]^{3-}$, $[FeF_6]^{3-}$, $[CrF_6]^{3-}$, and $[VF_6]^{3-}$ (46–51). Among these, only the t_{1u} modes ($a_{2u} + e_u$ in D_{4h}) are IR active. Consequently, the peaks observed in the IR spectrum at 686, 554, 395, and 277 cm^{-1} should correspond to the $a_{2u} + e_u$ modes of the $[MnF_4F_{2/2}]^{\infty}$ chain, given that a similar peak structure is observed in Na_2MnF_5. The highest frequencies at 686 and 554 cm^{-1} are assigned to a_{2u} and e_u modes, respectively, coming from the octahedral $t_{1u}{}^1$. In this assignment we assume that the axial Mn–F force constant is greater than the corresponding equatorial one in spite of the fact that the axial Mn–F distance, R_{as} (2.082 Å), is higher than the equatorial distance, R_{eq} (1.832 Å). Such a hardening of the axial Mn–F bond should be expected due to the presence of neighboring Mn^{3+} ions along the chain.

It must be noted, however, that the energies of the a_{2u} and b_{2u} ($t_{1u}{}^1$) modes for $Tl_2MnF_5 \cdot H_2O$ and Na_2MnF_5 are considerably higher than those of the MF_6^{3-} complexes, but they compare well with those found in tetra- or pentavalent ion complexes like VF_6^- (676, 538, 646, and 300 cm^{-1}), MnF_6^{2-} (592, 508, 620, and 335 cm^{-1}), or NiF_6^{2-} (555, 512, 648, and 332 cm^{-1}); the numbers in parentheses correspond to the a_{1g}, e_g, $t_{1u}{}^1$, and $t_{1u}{}^2$ vibrational energies, respectively (50). According to the previous arguments, the peaks at 395 and 277 cm^{-1} should be associated with the a_{2u} and e_u modes coming mainly from the octahedral $t_{1u}{}^2$ mode, thus confirming that none of these modes would be involved in the transition mechanism. Within this scheme, the octahedral a_{1g} amd e_g vibrational energies (a_{1g} and $a_{1g} + b_{1g}$ in D_{4h}) would lie between 550–700 cm^{-1} and 500–550 cm^{-1}, respectively. These estimates will be important in the analysis of the vibrational progressions in Section 4c.

4b2. Spin-forbidden transitions. There are two likely transition mechanisms for explaining the ED nature of the spin-forbidden transitions. The first mechanism is the spin–orbit interaction which can connect quintet and triplet states, together with the odd parity vibronic mechanism. The second one is the pair mechanism, only possible in exchange coupled systems (52, 53).

Considering our spin–orbit calculations and the results of Table 2, the first mechanism must be ruled out because the spin–orbit mixing coefficients between triplets and quintets would give rise to oscillator strengths at least two orders of magnitude less than the oscillator strengths of the spin-allowed transitions. Furthermore, their temperature dependences (Fig. 6) cannot be explained by the vibronic mechanism of Eq. [2].

On the other hand, this type of variation, also found in 1D antiferromagnetic compounds, is characteristic of exchange induced pairwise transitions (54, 55). Selection rules for pair transitions can be derived for the present case considering the $F_5MnFMnF_5$ dimer of D_{4h} symmetry by using the same procedure as Day and Dubicki to explain the polarization of the Mn (II) crystal field bands TMMC, CMMC, and CMCB (55). Pair states are formed

with symmetric and antisymmetric combinations of the total spin plus orbital products of single ion states. The ground state $^5B_{1g}(1) \times {}^5B_{1g}(2)$ gives rise to pair states of $^1A_{2u}$, $^3A_{1g}$, $^5A_{2u}$, $^7A_{1g}$, and $^9A_{2u}$. Consequently, ED transitions are allowed to pair states of either A_{1g} (or A_{2u}) or E_g (or E_u) depending on whether the light electric vector is parallel (π) or perpendicular (σ) to the fourfold axis of the dimer. Excited pair states having these symmetries are found for $^3B_{1g} \times {}^5B_{1g}$ and $^3E_g \times {}^5B_{1g}$, respectively, with spin values $S = 1$, 2, and 3. ED transitions to the single ion $^3A_{1g}$ states would also be allowed by this mechanism if we took into account the actual D_{2h} symmetry of the $[MnF_4F_{2/2}]^{\infty}$ chain.

The present selection rules are in agreement with the assignment given in Table 2. Moreover, the small shoulder observed in the spectrum at 21,700 cm^{-1} could be associated with either the $^5B_{1g} \rightarrow {}^3{}_bE_g$ or the $^5B_{1g} \rightarrow {}^3{}_aA_{1g}$ transitions, although we are not able to determine which mechanism, the exchange or the spin–orbit interaction, accounts for it.

The temperature dependence of the oscillator strengths of the $^5B_{1g} \rightarrow {}^3{}_aB_{1g}$ and $^5B_{1g} \rightarrow {}^3{}_bB_{1g}$ bands (Fig. 6) confirms the exchange nature of the transition mechanism. The variation $f(T)$ due to this mechanism, calculated theoretically several years ago by Ebara and Tanabe (54) for antiferromagnetic linear chain complexes using the classical approximation $S_i \rightarrow \infty$, is given by

$$f(T) = \frac{2f(0)}{(2S-1)}\left[S\,(U^2-1) + \frac{4S\,U(S+1) + (2S-1)UV}{2V}\right], \qquad [3]$$

where $f(0)$ is the 0-K oscillator strength, $U = \coth V - 1/V$, $V = 2JS(S+1)/K_BT$, S is the spin, and J (<0) is the intrachain exchange constant. This kind of variation accounts well for the observed intensities using $S = 2$ and $J \simeq 11$ cm^{-1}. This value of J is similar to that obtained from magnetic measurements $J = 15$ cm^{-1} in $Tl_2MnF_5 \cdot H_2O$. However, it must be pointed out that in the present case, J has been obtained with the condition that Eq. [3] has the intensity maximum at $T_M = 80$ K. In any case, the optical techniques prove to be useful for obtaining suitable values of J from the temperature dependences of the spin-forbidden transitions.

4c. Vibrational Structure; Analysis of the Huang–Rhys Factors

A noteworthy result of the present work is the observation of two vibrational progressions of 525 and 435 cm^{-1} in the $^5B_{1g} \rightarrow {}^5A_{1g}$ and $^5B_{2g}$ bands at low temperatures. The latter progression actually corresponds to the envelope of two coupled a_{1g} modes of 375 and 505 cm^{-1} as it is evidenced by the fine structure of Fig. 8. The number of vibrational quanta involved in each progression clearly indicates that the electron–phonon coupling in the $^5A_{1g}$ state is much stronger than in the $^5B_{2g}$ state. This conclusion could be anticipated from an analysis of the room temperature bandwidth of each band.

The coupling strength of the $^5A_{1g}$ band can be quantitatively estimated from the relative intensity, I_n, of each component of the progression and the second order moment, $M2$, of the low temperature band. For couplings to one mode within the harmonic approximation (56), these parameters are given by

$$I_n = I_0 e^{-S} S^n/n! \quad \text{and} \quad M2 = S(\hbar\omega)^2, \qquad [4]$$

where I_n is the intensity of the nth component of the progression, $I_0 = \sum_{n=0}^{\infty} I_n$ and S is the Huang–Rhys factor, which is related with the linear electron–phonon coupling coefficient, C, by (56)

$$S = \frac{1}{2}\left(\frac{C}{\hbar\omega}\right)^2 \frac{\hbar}{m\omega}. \qquad [5]$$

A Huang–Rhys factor $S = 9.0$ accounts for the band shape of the $^5B_{1g} \rightarrow {}^5A_{1g}$ transition (Fig. 7) as well as for the experimental 2nd order moment, $M2(9.5\ K) = 2.46 \times 10^6$ cm^{-2}. A value $S = 8.7$ is found if we include the factor E_n/E_0 in the intensity given by Eq. [4], which takes into account the variation of the oscillator strength with the transition energy (33). In either case, this unusually large value of S contrasts with those normally found in transition fluoride complexes, with $S \sim 1$–2, and in particular, with that corresponding to the $^5B_{1g} \rightarrow {}^5B_{2g}$ transition in $Tl_2MnF_5 \cdot H_2O$, of which the vibrational replicas of 505 and 375 cm^{-1} reveal Huang–Rhys factors $S \sim 1$–2 (Fig. 8).

The different ligand field dependence of the $^5B_{1g} \rightarrow {}^5A_{1g}$ and $^5B_{1g} \rightarrow {}^5B_{2g}$ transition energies, $\varepsilon_1 = \Delta_e$ and $\varepsilon_2 = 10Dq$, respectively, are responsible for the distinct Huang–Rhys factors associated with each transition. Semiempirical quantitative estimations of S can be made through Eq. [5] if we know both the linear electron–phonon coupling coefficient, C, and the nature of the corresponding coupled modes.

In MnF_6^{3-} (D_{4h}) complexes, there are only two possible totally symmetrical a_{1g} vibrations that can be linearly coupled to electronic transitions involving orbital singlets. These modes correspond to stretching motions of the axial and equatorial ligands against the Mn^{3+} ion. If we denote these modes by $Q_{eq} = (1/2)(r_1 + r_2 + r_3 + r_4)$ and $Q_{ax} = (1/\sqrt{2})(r_5 + r_6)$, where $r_i = R_i - R_i^0$ are the atomic displacements ($i = 1$ to 4 for equatorial ligands, and $i = 5$, 6 for the axial ones), then the normal modes of the complex,

Q_1 and Q_2, will be proper combinations of such modes,

$$Q_1 = \alpha Q_{eq} - \beta Q_{ax} \quad \text{and} \quad Q_2 = \beta Q_{eq} + \alpha Q_{ax}, \quad [6]$$

with $\beta = (1 - \alpha^2)^{1/2}$. The α value varies between 0 and 1 depending mainly on the difference between the axial and equatorial Mn–F force constants. The larger the difference between the force constants, the closer α is to 1.

The 525-cm^{-1} vibrational spacing observed in $^5B_{1g} \rightarrow {}^5A_{1g}$ obviously corresponds to the antiphase Q_1 mode if we take into account: (1) the energy of the Q_2 mode mainly associated to the octahedral a_{1g} mode would lie above 600 cm^{-1} as it has been discussed in Section 4b; (2) the $^5B_{1g} \rightarrow {}^5A_{1g}$ transition involves a spatial redistribution of the d electrons in such a way that the unoccupied one electron level, $d(x^2 - y^2)$, changes to the $d(3z^2 - r^2)$ level. This situation greatly increases the electronic repulsion around the equatorial ligands with respect to the axial ligands, thus favoring an increase of R_{eq} and a reduction of R_{ax} in the $^5A_{1g}$ excited state. In fact, this reflects the different ground state geometries found in CuF_6^{4-} complexes where either elongated or compressed D_{4h} distortions take place depending on whether the electronic ground state is $^2B_{1g}(x^2 - y^2)$ or $^2A_{1g}(3z^2 - r^2)$, respectively (40–42). Therefore, the Q_1 mode should be the most strongly coupled to the $^5B_{1g} \rightarrow {}^5A_{1g}$ transition.

In a single configurational mode model, the excited state potential energy is given by

$$\begin{aligned} E_{ex} &= E_0 - CQ_1 + \tfrac{1}{2}kQ_1^2 \\ &= E_0 - \tfrac{1}{2}kQ_{10}^2 + \tfrac{1}{2}k(Q_1 - Q_{10})^2, \end{aligned} \quad [7]$$

where E_0 is the energy difference between the ground and excited state potential energy for the ground state equilibrium geometry $Q_1 = 0$, k is the force constant of the Q_1 mode which is assumed to be the same for the ground and the excited states, Q_{10} is the excited state equilibrium coordinate, and C is the linear electron–phonon coupling constant which can be expressed as

$$C = -\left(\frac{\partial E_{ex}}{\partial Q_1}\right)_{Q_1=0}. \quad [8]$$

The crucial point for calculating the Huang–Rhys factor through Eq. [5] with this model is knowing the coefficient C. In this context, it is worth mentioning the interesting work performed by Moreno *et al.* (36) in order to explain the Huang–Rhys factors, $S(a_{1g})$, in octahedral transition metal complexes MX_6 (X = F, Cl, and Br). The present work attempts to generalize this model to complexes with nonequivalent axial and equatorial ligands.

For the $^5B_{1g} \rightarrow {}^5A_{1g}$ transition, C can be derived from the empirical relationship between the transition energy, ε_1, and the tetragonal parameter, x_D: $\varepsilon_1 = Bx_D$ with $B = 8.8 \times 10^4$ cm^{-1} in the present case. Then

$$\begin{aligned} C &= -\left(\frac{\partial E_{ex}}{\partial Q_1}\right)_{Q_1=0} \\ &= -\left(\left(\frac{\partial E_{ex}}{\partial R_{ax}}\right)\left(\frac{\partial R_{ax}}{\partial Q_1}\right) + \left(\frac{\partial E_{ex}}{\partial R_{eq}}\right)\left(\frac{\partial R_{eq}}{\partial Q_1}\right)\right)_{Q_1=0}, \end{aligned} \quad [9]$$

where

$$\left(\frac{\partial E_{ex}}{\partial R_{ax}}\right) = \frac{B}{R_{eq}}, \quad \left(\frac{\partial E_{ex}}{\partial R_{eq}}\right) = -\frac{B}{R_{eq}}\frac{R_{ax}}{R_{eq}},$$

$$\left(\frac{\partial R_{ax}}{\partial Q_1}\right) = -\frac{\beta}{\sqrt{2}}, \quad \text{and} \quad \left(\frac{\partial R_{eq}}{\partial Q_1}\right) = \frac{\alpha}{2}.$$

In these expressions it is assumed that E_{ex} has the same dependence as the energy of the absorption band maximum, ε_1, which is expected for strong couplings.

Employing Eqs. [5], [8], and [9] and taking $\hbar\omega = 525$ cm^{-1}, the fluorine mass, $m = 3.17 \times 10^{-23}$ g, $R_{eq} = 1.832$ Å, and $R_{ax} = 2.082$ Å, we obtain

$$S_{Q_1} = 14\left(1.136\frac{\alpha}{2} + \frac{\beta}{\sqrt{2}}\right)^2. \quad [10]$$

The Huang–Rhys factor S for the other $a_{1g}(Q_2)$ mode can be estimated from Eq. [10] by replacing α by β and β by $-\alpha$.

Note that the maximum S_{Q_1} values are found for $\alpha \approx 1/\sqrt{3}$, which obviously corresponds to the octahedral Jahn–Teller e_g mode, providing the greatest tetragonal distortion.

A relevant feature of the present analysis is that the experimental S value can be understood within this model, in which a correlation between static and dynamic properties has been established. In fact, for the two limiting cases, $\alpha = 0$ and $\alpha = 1$, we obtain $S_{Q_1} = 7.0$ and 4.5, respectively, which are of the same order as the experimental value. In particular, $S_{Q_1} = 9.0$ can be reproduced exactly if we take $\alpha = 0.92$ which corresponds to the *mainly* equatorial mode $Q_1 = 0.92\ Q_{eq} - 0.39\ Q_{ax}$.

From these results, we have calculated the excited state equilibrium geometry as well as the stabilization energy, the values of which are summarized in Table 3. Note that the excited state geometry is near a perfect octahedron ($x_D = 0.035$) but in no case is R_{eq} greater than R_{ax}, which evidences the crystalline constraint.

The absence of a progression associated with the mainly axial Q_2 mode is justified by the fact that the corresponding Huang–Rhys factor deduced from Eq. [10] taking $\alpha =$

TABLE 3

Spectroscopic Parameters of the $^5B_{1g} \rightarrow {}^5A_{1g}$ Transition and Local Geometry of the MnF_6^{3-} Complex in the Ground and the Excited $^5A_{1g}$ States

Transition: $^5B_{1g} \rightarrow {}^5A_{1g}$
$S = 9.0$
$\hbar\omega = 525\ cm^{-1}$
$C = 3.84 \times 10^4\ cm^{-1}/Å$
$Q_{10} = 0.246\ Å$
$-(1/2)k(Q_{10})^2 = 4700\ cm^{-1}$

	MnF_6^{3-} Geometry	
	$^5B_{1g}$ (ground state)	$^5A_{1g}$ (excited state)
R_{ax} (Å)	2.082	2.014
R_{eq} (Å)	1.832	1.945
R (Å)	1.92	1.97
x_D	0.136	0.035

Note. Top: Huang–Rhys factor, S; vibrational energy, $\hbar\omega$; linear electron–phonon coupling constant, C; excited state equilibrium normal coordinate, Q_{10}, and stabilization energy, $-(1/2)kQ_{10}^2$. Bottom: Ground state distances were measured by diffraction techniques (9), whereas excited state distances were obtained from Q_{10} and Eq. [6] for $\alpha = 0.92$ and $\beta = 0.39$.

0.39 and $\beta = -0.92$, would be $S_{Q_2} = 1.5$ if a vibrational spacing $\hbar\omega = 620\ cm^{-1}$ is assumed.

A precise analysis of the electron–phonon coupling cannot be performed in the $^5B_{1g} \rightarrow {}^5B_{2g}$ transition due to the lack of experimental data for determining C. In addition, the observation of two vibrational coupled modes of 505 and 375 cm^{-1} makes such a study difficult, especially considering that the presence of the latter mode is hard to conciliate with a D_{4h} symmetry because the energy of the remaining $a_{1g}(Q_2)$ mode should be much higher than 375 cm^{-1}. This mode, called Q_3, probably corresponds to the $Q'_{eq} = (1/2)(r_1 + r_2 - r_3 - r_4)$ mode of b_{1g} symmetry, since this is the only mode that transforms as a_g when the real D_{2h} symmetry of the MnF_6^{3-} complex is taken into account.

The weak couplings observed for these Q_1 and Q_3 modes in the $^5B_{1g} \rightarrow {}^5B_{2g}$ transition ($S \approx 1$–2) can be explained roughly by assuming that $10Dq \propto R_{eq}^{-p}$ with p close to 4. The linear electron–phonon coupling coefficients, C_i ($i = Q_1$ and Q_3), are then given by

$$C_i = -\left(\frac{\partial E_{ex}}{\partial Q_i}\right)_{Q_i=0} = -\left(\frac{\partial 10Dq}{\partial R_{eq}}\right)\left(\frac{\partial R_{eq}}{\partial Q_{eq}}\right)\left(\frac{\partial Q_{eq}}{\partial Q_i}\right). \quad [11]$$

It should be pointed out that such an approximation would be more precise as the normal mode descriptions for the $^5B_{2g}$ and $^5B_{1g}$ states become more similar to each other. These C_i values depend strongly on the u_i coefficients of the Q_{eq} mode for each a_{1g} mode, $Q_i = u_iQ_{eq} + v_iQ_{ax} + w_iQ'_{eq}$, since unlike Q_{ax} and Q'_{eq}, the mode Q_{eq} involves changes in R_{eq}, and is therefore linearly coupled to this transition. Taking $10Dq = 17{,}500\ cm^{-1}$, $\hbar\omega_1 = 505\ cm^{-1}$, $\hbar\omega_3 = 375\ cm^{-1}$, and $R_{eq} = 1.832$ Å, we find from Eqs. [5] and [11] that

$$S_{Q_1} = p^2\,0.155\,u_1^2 \quad \text{and} \quad S_{Q_3} = p^2\,0.378\,u_3^2. \quad [12]$$

Note that there is no coupling to the Q_3 mode (b_{1g}) within a D_{4h} symmetry since $u_3 = 0$, $v_3 = 0$, and $w_3 = 1$. But small departures from this symmetry cause an important enhancement of S_{Q_3} due to the lower frequency of this mode. Values of $u_1^2 = 0.8$ and $u_3^2 = 0.1$ would lead to values of $S_{Q_1} = 2$ and $S_{Q_3} = 0.6$ taking $p = 4$. This simple model accounts reasonably well for the experimental findings and also justifies the absence of replicas to the mainly axial Q_2 mode, since the crystal field distortions induced by the axial ligands do not modify $10Dq$ and consequently $C(Q_2) = 0$.

After this analysis, we assign the false origins at 150 and 200 cm^{-1} observed in the σ spectrum of Fig. 8 to the enabling ED odd parity e_u mode which splits under D_{2h} into $b_{2u} + b_{3u}$. Both peaks are associated to the same electronic origin because their intensities display the same temperature dependence as the sharp peak at 16,586 cm^{-1}.

An interesting feature is the behavior of this sharp origin, for which the intensity seems to be very sensitive to the 3D magnetic ordering. Efforts to detect the pure exciton line in both π and σ polarizations were unsuccessful. The temperature dependence of this peak (Fig. 9) resembles that followed by cold exciton–magnon peaks in antiferromagnets, though these peaks have always been detected in transitions involving states of different spin parity. In particular, a very similar behavior has been found by Güdel *et al.* (57) in the $CsVBr_3$ antiferromagnet. The exciton–magnon line intensity of the $^4A_2 \rightarrow {}^2T_2$ transition of V^{2+} was seen to drop out just above the Néel temperature following the same temperature dependence as the sublattice magnetization. These behaviors have also been found in 3D antiferromagnets such as MnF_2 (58) and $RbMnF_3$ (59) and explained theoretically by Tanabe *et al.* (59, 60) by means of the exciton–magnon coupling mechanism.

In the present system, the intensity variation for both *cold* and *hot* components are consistent with this magnonic mechanism and the Néel temperature derived from this curve would be close to $T_N = 28$ K. It should be noted, however, that although the sharp peak decreases like T^2 up to 25 K, in no case does its variation reflect the sublattice magnetization measured through the intensity of the (101) magnetic Bragg peak (9).

Finally, it is important to point out the poor sensitivity of the triplet peaks for detecting the 3D magnetic ordering. Neither the intensity nor the peak energy gives clear evi-

dence of such an ordering within our experimental accuracy. But some evidence has been found in the temperature dependence of the halfwidth of the first $^5B_{1g} \rightarrow {}^3_a B_{1g}$ peak at 19,600 cm^{-1} (Fig. 10) which shows different behaviors above and below T_N. Further work using high resolution spectroscopy would be useful to clarify the nature of the triplet structure of the two $^5B_{1g} \rightarrow {}^3B_{1g}$ spin-forbidden transitions as well as to analyze the influence of the antiferromagnetic order.

5. CONCLUSIONS

The most relevant conclusions of the present investigation are the following:

(1) A correlation between the spectroscopic parameters and the local structure of the MnF_6^{3-} complexes has been established. The splitting of the parent ^5E_g and $^5T_{2g}$ octahedral states, Δ_e and Δ_t, shows a linear dependence on the tetragonal parameter, x_D: $\Delta_e = 8.8 \times 10^4\, x_D$ and $\Delta_t = 2.2 \times 10^4\, x_D$ (in cm^{-1} units).

(2) The spin-allowed crystal field bands are ED vibronically assisted by the odd parity b_{2u} (165 cm^{-1}) and e_u (200 cm^{-1}) modes while the intensity of the spin-forbidden bands is enabled by a pairwise exchange mechanism. The temperature dependence of the oscillator strength, $f(T)$, and the type of polarization exhibited by these bands confirm the assignment and the proposed transition mechanisms.

(3) The vibrational progressions observed in the $^5B_{1g} \rightarrow {}^5A_{1g}$ band (525 cm^{-1}) and in the $^5B_{1g} \rightarrow {}^5B_{2g}$ (505 and 375 cm^{-1}) reflect coupling to totally symmetrical a_{1g} modes, which mainly involve stretching motions of the equatorial ligands. The large difference between the corresponding Huang–Rhys factors $S = 9$ and $S \approx 1$–2 is explained by correlating static and dynamic properties of the MnF_6^{3-} complexes. The absence of progressions of the highest energy a_{1g} mode, Q_2, in these transitions is explained by the small linear electron–phonon coupling coefficients and its high frequency, $\hbar\omega \approx 620$ cm^{-1}.

(4) There is an exciton–magnon peak in the low temperature spectra, for which the intensity temperature dependence gives evidence of the 3D magnetic ordering, thus providing a good determination of the Néel temperature for this $Tl_2MnF_5 \cdot H_2O$ compound. On the other hand, these dependences for the spin-forbidden bands allow us to obtain suitable values of the intrachain exchange constant, $J = 11$ cm^{-1}.

APPENDIX

Water Absorption

The intense OA band at 5000 cm^{-1} and the weaker one at 6450 cm^{-1} are associated with vibrational overtones of the water molecule. Bands around 5000 cm^{-1} were also observed in the $(NH_4)_2MnF_5$ spectrum, which were assigned analogously by Dingle to overtones of the NH_4 vibrations (27). In the present case, the proposed assignment is supported by the fact that none of these bands is observed in the Na_2MnF_5 anhydrous compound (inset of Fig. 2). In addition, recent studies on $MnXO_4 \cdot H_2O$ (X = P, As) and the corresponding deuterated compounds indicate that these bands disappear after crystal dehydration (43).

In $Tl_2MnF_5 \cdot H_2O$, we assign these bands to combinations of the ν_2 and ν_3 fundamentals where ν_2 and ν_3 as well as ν_1 are the vibrational frequencies of the a_1 (bending), b_1 (stretching), and a_1 (stretching) modes, respectively, of the H_2O molecule (C_{2v} symmetry). The intense band is assigned to $\nu_2 + \nu_3$ and the weaker one to $2\nu_2 + \nu_3$ for the following reasons: (1) the experimental peaks at 5000 and 6450 cm^{-1} are close to the sums $\nu_2 + \nu_3 \simeq 5020$ cm^{-1} and $2\nu_2 + \nu_3 = 6670$ cm^{-1}, of the respective fundamentals, $\nu_1 = 3273$, $\nu_2 = 1648$, and $\nu_3 = 3375$ cm^{-1}, obtained from the IR spectrum of Fig. 11. As in water vapor (44), the highest frequency was assigned to the ν_3 mode. However, in $Tl_2MnF_5 \cdot H_2O$, ν_1 and ν_3 are smaller than in vapor, where $\nu_1 = 3652$, and $\nu_3 = 3756$ cm^{-1}, while ν_2, on the other hand, is larger than the vapor value, $\nu_2 = 1595$ cm^{-1} (44). This reflects the softening of the H_2O stretching modes usually observed in solids due to the presence of hydrogen bonds. The hardening of ν_2 could be associated with the F···H bonds in this structure, which impedes the bending of the H–O–H bonds (Fig. 1). (2) In general, the H_2O vibrations are completely polarized in the plane of the molecule either parallel (combinations of a_1 modes) or perpendicular (any combination involving the b_1 mode) to the twofold axis of the molecule. This behavior is indeed observed in the spectra of Fig. 5. The fact that those bands involving the b_1 mode appear only in the π spectrum cleary indicates that the symmetry axis of the water molecules must be perpendicular to the **c** axis, in agreement with the crystallographic structure obtained by neutron diffraction. Furthermore, the proposed overtones are also the same ones observed in H_2O vapor in this spectral region (44).

ACKNOWLEDGMENTS

We are indebted to R. Valiente for helping us with the Yeung and Rudowicz calculation programs. P. N. is very grateful to Dr. Alain Tressaud at the Laboratoire de Chimie du Solide (Université de Bordeaux) for introducing him to solid state chemistry and for fruitful discussions.

REFERENCES

1. P. Kohler, W. Massa, D. Reinen, B. Hoffman, and R. Hoppe, *Z. Anorg. Allg. Chem.* **446,** 131 (1978).
2. A. Tressaud and J. M. Dance, *Struct. Bonding* **52,** 87 (1982).
3. W. Massa and D. Babel, *Chem. Rev.* **88,** 275 (1988).

4. J. Pebler, W. Massa, H. Lass, and B. J. Ziegler, *J. Solid State Chem.* **71,** 87 (1987).
5. P. Nuñez, J. Darriet, P. Bukovec, A. Tessaud, and P. Hagenmuller, *Mater. Res. Bull.* **22,** 661 (1987).
6. F. Palacio, M. Andres, C. Esteban-Calderon, M. Martinez-Ripoll, and S. Garcia Blanco, *J. Solid State. Chem.* **76,** 33 (1988).
7. F. Palacio, M. Andres, J. Rodriguez-Carvajal, and J. Pannetier, *J. Phys. Condens. Matter* **3,** 2340 (1991).
8. W. Massa and Burk, *Z. Anorg. Allg. Chem.* **516,** 119 (1984).
9. P. Nuñez, A. Tressaud, J. Darriet, P. Hagenmuller, G. Hahn, G. Frenzen, W. Massa, D. Babel, A. Boireau, and J. L. Soubeyroux, *Inorg. Chem.* **31,** 770 (1992).
10. R. Sears and J. L. Hoard, *J. Chem. Phys.* **50,** 1066 (1969).
11. W. Massa, *Acta Crystallogr. Sect. C* **42,** 644 (1986).
12. M. Molinier, W. Massa, S. Khairoun, A. Tressaud, and J. L. Soubeyroux, *Z. Naturforsch.* **46b,** 1669 (1991).
13. M. Molinier and W. Massa, *Z. Naturforsch.* **47b,** 783 (1992).
14. P. Nuñez, A. Tressaud, J. Grannec, P. Hagenmuller, W. Massa, D. Babel, A. Boireau, and J. L. Soubeyroux, *Z. Anorg. Allg. Chem.* **609,** 71 (1992).
15. D. Babel, *Z. Anorg. Allg. Chem.* **336,** 200 (1965).
16. G. C. Allen, G. A. M. El-Sharkawy, and K. D. Warren, *Inorg. Chem.* **11,** 2538 (1971).
17. U. Englich, W. Massa, and A. Tressaud, *Acta Crystallogr., Sect. C* **48,** 6 (1992).
18. W. Massa and M. Steiner, *J. Solid State Chem.* **32,** 137 (1980).
19. F. Palacios, M. C. Moron, and J. Rodriguez, "Spanish Neutron Research using Neutron Scattering Techniques," (J. C. Gomez-Sal, F. Rodríguez, J. M. Barandiaran, F. Plazaola, and T. Rojo, Eds.), p. 160. University of Cantabria, Spain, 1991.
20. P. Bukovec and V. Kaucic, *Acta Crystallogr., Sect. B* **34,** 3339 (1978).
21. J. R. Gunther, J. P. Matthieu, and H. R. Oswald, *Helv. Chim. Acta* **61,** 328 (1978).
22. F. Palacio, M. Andres, R. Horne, and A. J. Van Duyneveldt, *J. Magn. Magn. Mater.* **54–57,** 1487 (1986).
23. F. Palacio, M. Andres, D. Van der Noort, and A. J. Van Duyneveldt, *J. Phys. C-8* **49,** 819 (1988).
24. P. Nuñez, A. Tressaud, F. Hahn, W. Massa, D. Babel, A. Boireau, and J. L. Soubeyroux, *Phys. Status Solidi A* **127,** 505 (1991).
25. F. Hahn and W. Z. Massa, *Z. Naturforsch.* **45b,** 1341 (1990).
26. D. Oelkrug, *Struct. Bonding* **9,** 1 (1971).
27. R. Dingle, *Inorg. Chem.* **4,** 1287 (1965).
28. T. S. Davis, J. P. Fackler, and M. J. Weeks, *Inorg. Chem.* **7,** 1991 (1968).
29. M. N. Bhattacharjee, M. K. Chaudhuri, H. S. Dasgupta, and A. Kathipri, *Polyhedron* **4,** 621 (1985).
30. M. Andres, Thesis, University of Zaragoza, Spain, 1989.
31. P. Day, A. K. Gregson, and D. H. Leech, *Phys. Rev. Lett.* **30,** 19 (1973).
32. Y. Y. Yeung and C. Rudowicz, *Comput. Chem.* **16,** 207 (1992).
33. A. B. P. Lever, "Inorganic Electronic Spectroscopy," 2nd ed., Chapt. I. Elsevier, New York, 1986.
34. E. Francisco, M. Florez, Z. Barandiaran, G. Fernandez Rodrigo, V. Luaña, J. M. Recio, M. Bermejo, L. Seijo, and L. Pueyo, *Cryst. Lattice Defects Amorphous Mater.* **15,** 45 (1987).
35. V. Luaña, M. Bermejo, M. Florez, J. M. Recio and L. Pueyo, *J. Chem. Phys.* **90,** 6409 (1989).
36. M. Moreno, M. T. Barriuso, and J. A. Aramburu, *J. Phys.: Condens. Matter* **4,** 9481 (1992).
37. F. Rodriguez and M. Moreno, *J. Chem. Phys.* **84,** 692 (1986).
38. F. Rodriguez, M. Moreno, A. Tressaud and J. P. Chaminade, *Cryst. Lattice Defects Amorphous Mater.* **16,** 221 (1987).
39. M. C. Marco de Lucas, F. Rodriguez, and M. Moreno, *J. Phys. Condens. Matter* **5,** 1437 (1993).
40. M. J. Riley, L. Dubicki, G. Moran, E. R. Krausz, and I. Yamada, *Chem. Phys.* **145,** 363 (1990).
41. D. Reinen, G. Steffen, M. A. Hitchman, H. Stratemeier, L. Dubicki, E. Krausz, M. J. Riley, H. E. Mathies, K. Recker, and F. Wallrafen, *Chem. Phys.* **155,** 117 (1991).
42. K. Finnie, L. Dubicki, E. R. Krausz, and M. J. Riley, *Inorg. Chem.* **29,** 3908 (1990).
43. M. A. Garcia-Aranda, Thesis, University of Malaga, Spain, 1992.
44. G. Herzberg, "Molecular Spectra and Molecular Structure," Chapt. III. Van Nostrand–Reinhold, New York, 1945.
45. H. U. Gudel and T. R. Snellgrove, *Inorg. Chem.* **17,** 1617 (1978).
46. L. Dubicki, J. Ferguson, and B. Von Oosterhout, *J. Phys. C* **13,** 2791 (1980).
47. M. C. Marco de Lucas, F. Rodriguez, J. M. Dance, M. Moreno, and A. Tressaud, *J. Lumin.* **48 & 49,** 553 (1991).
48. A. Payne, L. L. Chase, and G. D. Wilke, *J. Lumin.* **44,** 167 (1989).
49. F. Rodriguez, H. Riesen, and H. U. Gudel, *J. Lumin.* **50,** 101 (1991).
50. K. Nakamoto, "Infrared and Raman Spectra of Inorganic and Coordination Compounds," 4th ed., Chapt. II. Wiley, New York, 1986.
51. C. Pique, A. Bulou, M. C. Moron, R. Burriel, J. L. Fourquet, and M. Rousseau, *J. Phys. Condens. Matter* **2,** 8277 (1990).
52. H. U. Gudel, "Magneto-structural Correlations in Exchange Coupled Systems," (R. D. Willet, D. Gatteschi, and O. Kahn, Eds.), p. 127. Reidel, Dordrecht, 1985.
53. P. J. McCarthy and H. U. Gudel, *Coord. Chem. Rev.* **88,** 69 (1988).
54. K. Ebara and Y. Tanabe, *J. Phys. Soc. Jpn.* **36,** 93 (1974).
55. P. Day and L. Dubicki, *J. Chem. Soc., Faraday Trans. 2,* 363 (1973).
56. D. B. Fitchen, "Physics of Colour Centers," (W. B. Fowler, Ed.), Chapt. V. Academic Press, New York, 1968.
57. A. Hauser and H. U. Gudel, *Chem. Phys. Lett.* **82,** 72 (1981).
58. R. L. Green, D. D. Sell, W. M. Yen, and A. L. Schallow, *Phys. Rev. Lett.* **15,** 656 (1965).
59. K. Shinagawa and Y. Tanabe, *J. Phys. Soc. Jpn.* **30,** 1280 (1971).
60. T. Fujiwara and Y. Tanabe, *J. Phys. Soc. Jpn.* **32,** 9120 (1972).